

---

# Fuse It or Lose It: Deep Fusion for Multimodal Simulation-Based Inference

---

Marvin Schmitt<sup>1</sup> Stefan T. Radev<sup>2</sup> Paul-Christian Bürkner<sup>3</sup>

## Abstract

We present multimodal neural posterior estimation (MultiNPE), a method to integrate heterogeneous data from different sources in simulation-based inference with neural networks. Inspired by advances in deep fusion learning, it empowers researchers to analyze data from different domains and infer the parameters of complex mathematical models with increased accuracy. We formulate multimodal fusion approaches for MultiNPE (early, late, hybrid) and evaluate their performance in three challenging experiments. MultiNPE not only outperforms single-source baselines on a reference task, but also achieves superior inference on scientific models from neuroscience and cardiology. We systematically investigate the impact of partially missing data on the different fusion strategies. Across our experiments, late and hybrid fusion techniques emerge as the methods of choice for practical applications of multimodal simulation-based inference.

## 1. Introduction

Simulations have become a fundamental tool to model complex phenomena across the sciences and engineering (Lavin et al., 2021). High-fidelity simulation programs implement theories by domain experts. Their behavior is controlled by *parameters*  $\theta$  and latent program states  $\xi$  (Cranmer et al., 2020). Typically, the simulation parameters  $\theta$  are unknown and must be inferred from observable data  $\mathcal{D}$  to understand the underlying mechanisms. The probabilistic (Bayesian) approach to this *inverse problem* aims to obtain the posterior distribution  $p(\theta | \mathcal{D}) \propto p(\theta) p(\mathcal{D} | \theta)$ , given a prior  $p(\theta)$  and observable data  $\mathcal{D}$ . While sampling synthetic data from a mechanistic simulator is typically easy, the likelihood  $p(\mathcal{D} | \theta)$  is generally only *implicitly* defined via a high-dimensional integral over all possible execution paths  $\xi$  of the simulator, which is analytically intractable for complex simulators of practical interest

(Cranmer et al., 2020). This disqualifies gold-standard algorithms, such as MCMC (Neal, 2011) or variational inference (Blei et al., 2017), which rely on the ability to evaluate the likelihood for any pair  $(\theta, \mathcal{D})$ . In contrast, simulation-based inference (SBI) methods (Sisson et al., 2018) relax this requirement and only require synthetic tuples  $(\theta, \mathcal{D})$  from the simulation program.

The family of neural posterior estimation (NPE) algorithms uses a conditional neural density estimator (e.g., normalizing flow; Papamakarios et al., 2021) to learn a surrogate  $q_\phi(\theta | \mathcal{D})$  for the posterior  $p(\theta | \mathcal{D})$  in a simulation-based training phase. Subsequently, the upfront training is *amortized* by nearly instant posterior inference: For a *new* observed data set  $\mathcal{D}_o$ , the neural network can instantly sample from the approximate posterior  $q_\phi(\theta | \mathcal{D}_o)$ .

Neural SBI is still in its infancy, and we extend its repertoire to the practically relevant class of mechanistic *multiphase models*, where a set of shared parameters influences heterogeneous sources of data via distinct simulators. Relevant examples include computational models in cardiovascular precision medicine (Wehenkel et al., 2023), or integrative models of decision making and neural activity in the cognitive sciences (Ghadery-Kangavari et al., 2023). SBI currently lacks the tools to properly analyze such multimodal data. Our paper addresses this fundamental limitation of NPE with the following main contributions:

1. We present multimodal neural posterior estimation (MultiNPE), which enables the integration of multimodal data into simulation-based inference methods.
2. We develop variations of MultiNPE, translating advances in attention-based deep fusion learning into probabilistic machine learning with neural networks.
3. We demonstrate that MultiNPE outperforms existing SBI methods on a 10D reference task and two scientific models from neuroscience and cardiology.

## 2. Preliminaries

This section gives a brief overview of neural posterior estimation, learned summary statistics, and multi-head attention. Acquainted readers can fast-forward to [Section 3](#).

---

<sup>1</sup>University of Stuttgart <sup>2</sup>Rensselaer Polytechnic Institute  
<sup>3</sup>TU Dortmund University. Correspondence to: Marvin Schmitt  
 <mail.marvinschmitt@gmail.com>.

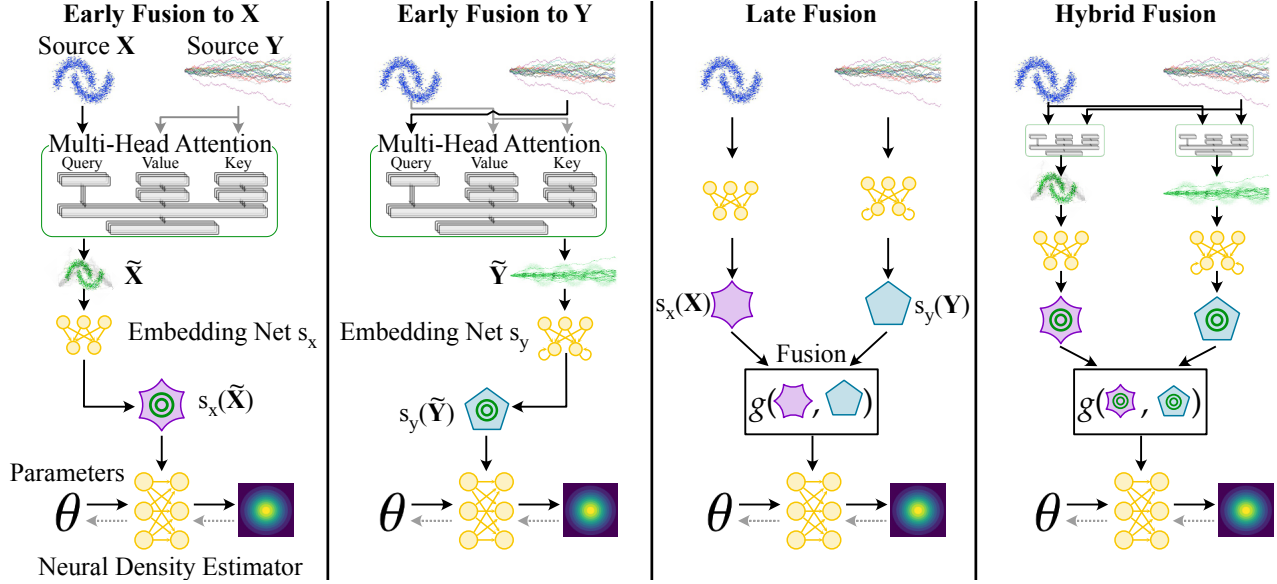


Figure 1: Multimodal neural posterior estimation (MultiNPE) is a family of principled methods to integrate information from multiple heterogeneous data sources  $\mathbf{X}$  and  $\mathbf{Y}$  in simulation-based inference (SBI). Early fusion to  $\mathbf{X}$  uses multi-head attention with  $\mathbf{X}$  as query and  $\mathbf{Y}$  as both key and value, arriving at the cross-informed  $\tilde{\mathbf{X}}$ . Equivalently, early fusion to  $\mathbf{Y}$  uses  $\mathbf{Y}$  as query and yields  $\tilde{\mathbf{Y}}$ . Both early fusion variants use a neural network  $s_\cdot(\cdot)$  to learn a representation of the fused data. In contrast, late fusion learns separate embeddings  $s_x(\mathbf{X})$  and  $s_y(\mathbf{Y})$ , and then fuses the embeddings. Hybrid fusion combines both worlds by using a symmetrical cross-shaped multi-head attention like in early fusion, followed by separate embeddings and a late fusion step. See Section 3 for a more formal specification.

## 2.1. Neural posterior estimation

The inverse problem of approximating the posterior distribution in SBI can be tackled by targeting the posterior directly with a class of algorithms called neural posterior estimation (NPE). NPE uses a conditional neural density estimator  $q_\phi(\boldsymbol{\theta} | \mathcal{D})$  with neural network parameters  $\phi$ , such as a normalizing flow (Papamakarios et al., 2021), score-matching networks (Geffner et al., 2022; Sharrock et al., 2022), flow matching (Dax et al., 2023), or consistency models (Schmitt et al., 2023). Here, we focus on normalizing flows due to their fast single-pass inference and simple training, even though our approach for multimodal SBI translates seamlessly to other backbone neural density estimators (see Experiment 3 for flow matching).

A conditional normalizing flow learns a map from a simple base distribution (e.g., a unit Gaussian) to the target posterior  $p(\boldsymbol{\theta} | \mathcal{D})$ . The normalizing flow is optimized by minimizing the Kullback-Leibler (KL) divergence between the true posterior  $p(\boldsymbol{\theta} | \mathcal{D})$  and its approximation  $q_\phi(\boldsymbol{\theta} | \mathcal{D})$  via the maximum likelihood objective  $\mathbb{E}_{p(\boldsymbol{\theta})p(\mathcal{D} | \boldsymbol{\theta})}[-\log q_\phi(\boldsymbol{\theta} | \mathcal{D})]$ . The normalizing flow can be trained on samples  $(\boldsymbol{\theta}, \mathcal{D})$  from the joint distribution  $p(\boldsymbol{\theta}, \mathcal{D}) = p(\boldsymbol{\theta})p(\mathcal{D} | \boldsymbol{\theta})$ , which corresponds to generating data from a simulation program. Once the normalizing flow has been trained, it can instantly sample from the

posterior  $q_\phi(\boldsymbol{\theta} | \mathcal{D}_o)$  for new observed data  $\mathcal{D}_o$  with a single pass through the trained networks. By recasting costly probabilistic inference as a neural network prediction task, normalizing flows achieve *amortized inference* across the prior predictive distribution  $p(\mathcal{D})$ .

## 2.2. Embedding networks for end-to-end learned summary statistics

In Bayesian inference, the data  $\mathcal{D}$  can be replaced by *sufficient* summary statistics  $s_*(\mathcal{D})$  without altering the posterior:  $p(\boldsymbol{\theta} | \mathcal{D}) = p(\boldsymbol{\theta} | s_*(\mathcal{D}))$ . Ideally,  $s_*$  is also low-dimensional, achieving lossless compression with regard to  $\boldsymbol{\theta}$  conditional on  $\mathcal{D}$ . While low-dimensional sufficient summary statistics are notoriously difficult to find for complex problems, the task of constructing approximate summary statistics  $s(\mathcal{D})$  with  $p(\boldsymbol{\theta} | \mathcal{D}) \approx p(\boldsymbol{\theta} | s(\mathcal{D}))$  has been extensively studied for approximate Bayesian inference. Within neural SBI, neural networks are employed to learn embeddings of the data  $\mathcal{D}$  in tandem with the posterior approximator (Radev et al., 2020a;b; Chen et al., 2021; Chan et al., 2018; Huang et al., 2023). These embedding networks  $s_\psi$  learn a transformation that aims to obtain low-dimensional statistics of the data  $\mathcal{D}$  which are sufficient for posterior inference (not necessarily for reconstructing the data). The embedding networks are parameterized by learnable neural network weights  $\psi$ . The NPE loss with *learned embed-*

dings  $s_\psi(\mathcal{D})$  minimizes the objective

$$\mathcal{L}(\phi, \psi) = \mathbb{E}_{p(\theta) p(\mathcal{D} | \theta)} [-\log q_\phi(\theta | s_\psi(\mathcal{D}))], \quad (1)$$

and we omit the network weights  $\psi$  for brevity. The concrete architecture of the embedding network should match the probabilistic symmetries of the data. For example, *i.i.d.* data sets can be embedded with a permutation-invariant neural network, such as a DeepSet (Zaheer et al., 2017) or an attention-based set transformer (Lee et al., 2019). Similarly, time series data require a neural architecture which respects their probabilistic structure in time, such as an LSTM (Hochreiter & Schmidhuber, 1997) or an attention-based temporal fusion transformer (Wen et al., 2023).

### 2.3. Multi-head attention

Attention mechanisms play a crucial role in machine learning, and one of the most notable architectures that has revolutionized the field is the Transformer (Vaswani et al., 2017). The Transformer introduces a highly effective mechanism for capturing dependencies and relationships within sequences of data, making it particularly well-suited for tasks such as natural language processing (Vaswani et al., 2017) or computer vision (Dosovitskiy et al., 2021). The core of the Transformer’s attention mechanism is the scaled dot-product attention, which is defined as

$$\text{Attention}(Q, V, K) = \text{softmax}\left(\frac{QK^\top}{\sqrt{d_k}}\right)V, \quad (2)$$

with queries  $Q$ , values  $V$ , and keys  $K$  of dimension  $d_K$ . To enhance the model’s ability to capture different types of relationships and dependencies in the data, the Transformer employs multi-head attention (MHA). MHA enables the model to jointly attend to information from different subspaces of the data across multiple attention heads. Each attention head is a separate instance of the scaled dot-product attention mechanism (Equation 2), and their outputs are combined using learnable linear transformations to produce the final multi-head attention output,

$$\begin{aligned} \text{MHA}(Q, V, K) &= [\text{head}_1, \dots, \text{head}_h]W^O \\ \text{head}_i &= \text{Attention}(QW_i^Q, KW_i^K, VW_i^V) \end{aligned} \quad (3)$$

where  $h$  represents the number of attention heads, and  $W^O$ ,  $W_i^Q$ ,  $W_i^K$ ,  $W_i^V$  are learnable weight matrices for combining the outputs of individual attention heads. The multi-head attention mechanism allows the Transformer model to encode patterns and relationships in the data, making it highly effective for a range of sequence-to-sequence tasks.

## 3. Method

### 3.1. Simulation paradigm and notation

In this section, we consider multimodal test data  $\mathcal{D}_o = \{\mathbf{X}_o, \mathbf{Y}_o\}$  from two sources<sup>1</sup>, as well as a simulation program capable of generating synthetic data  $\mathcal{D} = \{\mathbf{X}, \mathbf{Y}\}$ . An instance of either data source can consist of multiple observations, e.g. patients in a medical trial, or discrete steps in a time series. We use  $N$  for the cardinality of the first source,  $\mathbf{X} \equiv \{\mathbf{x}_n\}_{n=1}^N$ , and  $M$  for the cardinality of the second source  $\mathbf{Y} \equiv \{\mathbf{y}_m\}_{m=1}^M$ . Following the standard notation in SBI, the neural networks are trained on a total of  $K$  data sets  $\{\mathcal{D}^{(k)}\}_{k=1}^K \equiv \{\{\mathbf{X}^{(k)}, \mathbf{Y}^{(k)}\}\}_{k=1}^K$ .  $K$  is also called the *simulation budget*. To shorten notation, we drop the data set index  $k$  when it is not relevant to the context. The sub-programs generating the individual data modalities are based on common parameters  $\theta$  as well as domain-specific parameters  $\theta_x, \theta_y$ . Using the verbose notation once to avoid ambiguity, the joint forward model  $p(\theta, \theta_x, \theta_y, \mathbf{X}, \mathbf{Y})$  for a single data set  $\mathcal{D}^{(k)} = \{\mathbf{X}^{(k)}, \mathbf{Y}^{(k)}\}$  is defined as:

$$\begin{aligned} \theta^{(k)}, \theta_x^{(k)}, \theta_y^{(k)} &\sim p(\theta, \theta_x, \theta_y) \\ \mathbf{x}_n^{(k)} &\sim p(\mathbf{x} | \theta^{(k)}, \theta_x^{(k)}), \quad n = 1, \dots, N \\ \mathbf{y}_m^{(k)} &\sim p(\mathbf{y} | \theta^{(k)}, \theta_y^{(k)}), \quad m = 1, \dots, M \end{aligned} \quad (4)$$

The result of sampling from this forward model  $K$  times is a set of  $K$  tuples of parameters and data sets,

$$\left\{ \underbrace{\{\theta^{(k)}, \theta_x^{(k)}, \theta_y^{(k)}\}}_{\text{Parameters}}, \underbrace{\{\mathbf{X}^{(k)}, \mathbf{Y}^{(k)}\}}_{\text{Data } \mathcal{D}^{(k)}} \right\}_{k=1}^K,$$

and the inverse problem consists in inferring all unknown parameters from the data. Because SBI uses a synthetic simulation program, the ground-truth parameter values are available during the training phase. In the inference (test) phase however, the ground truth parameters of the test data  $\mathcal{D}_o = \{\mathbf{X}_o, \mathbf{Y}_o\}$  are naturally unknown and need to be estimated by the generative network  $q_\phi(\theta, \theta_x, \theta_y | \mathbf{X}, \mathbf{Y})$ .

### 3.2. Necessity of principled deep fusion

Consider the scenario where we estimate a single shared parameter  $\theta$  that manifests itself in both an *i.i.d.* data set  $\mathbf{X} \sim p(\mathbf{X} | \theta)$  and a Markovian time series  $\mathbf{Y} \sim p(\mathbf{Y} | \theta)$ . The fundamentally different probabilistic systems for  $\mathbf{X}$  and  $\mathbf{Y}$  cannot possibly be efficiently learned with a single neural architecture because (i) a permutation invariant network is suited for *i.i.d.* data but cannot capture the autoregressive structure of a time series; and (ii) a time series

<sup>1</sup>We limit this description to two sources for brevity. As discussed in Section 3.4 and illustrated in Experiment 3, a more involved layout of attention blocks can readily fuse more sources in a similar fashion.

network can fit time series but cannot efficiently learn the permutation-invariant structure of *i.i.d.* data. As a consequence, we need separate information processing streams to accommodate the specific structure of each data source. Yet, the neural density estimator  $q_\phi$  demands a fixed-length conditioning vector  $s(\mathcal{D})$ . We serve both requirements simultaneously: First, we process the heterogeneous streams of information  $\mathbf{X}$  and  $\mathbf{Y}$  with dedicated architectures. Second, we integrate the information into a fixed-length embedding before it enters the neural density estimator.

When either of the simulators has no individual parameters, we revert to a special case of Equation 4 and our method remains unaltered (see **Experiments 1** and **3**). However, if there are no *shared* parameters, a multimodal architecture will clearly not have any advantage over separate NPE algorithms for the two sub-problems.

### 3.3. Fusion strategies

The integration of information from different data sources is called *fusion*, and there are multitudes of options for *how* and *when* the fusion happens (see Figure 1). Previous work on deep fusion learning differentiates early fusion, late fusion, and hybrid approaches (Atrey et al., 2010; Gunes & Piccardi, 2005; Zhang et al., 2019). Our embedding network  $s(\cdot)$  corresponds to the decision function in the standard multimodal machine learning taxonomy.

**Early fusion** performs the fusion step as early as possible, ideally directly on the raw data (see Figure 1 panel 1 and 2). We implement this via cross-attention (Lu et al., 2019; Murahari et al., 2020) between the input modalities  $\mathbf{X}$  and  $\mathbf{Y}$ . Concretely, we use multi-head attention (Vaswani et al., 2017) with queries  $Q$ , values  $V$ , and keys  $K$ . The data inputs  $\mathbf{X}$  and  $\mathbf{Y}$  can differ with respect to their dimensions but the shapes of  $V$  and  $K$  must align for multi-head attention. Thus, we select one of the data sources ( $\mathbf{X}$  or  $\mathbf{Y}$ ) as query  $Q$  while the other one acts as both value  $V$  and key  $K$ . In **Experiment 1**, we illustrate that the choice of data sources for  $Q$  and  $V, K$  influences the results when the data sources  $\mathbf{X}$  and  $\mathbf{Y}$  differ with respect to their informativeness. After the attention-based fusion step, we pass the output of the multi-head attention block to a suitable embedding network  $s(\cdot)$  to provide a proper input for the conditional neural density estimator  $q_\phi$ . In summary, the information flow in early fusion is

$$s(\mathcal{D}) = \begin{cases} s_x\left(\text{MHA}(Q(\mathbf{X}), V(\mathbf{Y}), K(\mathbf{X}))\right) & \leftarrow \text{E. F. to } \mathbf{X} \\ s_y\left(\text{MHA}(Q(\mathbf{Y}), V(\mathbf{X}), K(\mathbf{X}))\right) & \leftarrow \text{E. F. to } \mathbf{Y} \end{cases} \quad (5)$$

where  $\text{MHA}(Q, V, K)$  denotes multi-head attention (see Section 2.3) and E. F. is an abbreviation for early fusion.

**Late fusion** is a diametrical approach where the fusion

step happens at a later stage (see Figure 1 panel 3). In SBI with learnable embeddings, this translates to fusion immediately before passing the final embedding to the conditional neural density estimator as conditioning variables. At this stage, both data inputs have already been embedded into learned summary statistics  $s_x(\mathbf{X})$  and  $s_y(\mathbf{Y})$  with fixed lengths each. Thus, late fusion can be achieved by simply concatenating the embeddings,  $s(\mathcal{D}) = g(s_x(\mathbf{X}), s_y(\mathbf{Y})) = [s_x(\mathbf{X}), s_y(\mathbf{Y})]$ , which is a common choice for the fusion function  $g$  (Atrey et al., 2010; Gunes & Piccardi, 2005; Zhang et al., 2019).

**Hybrid fusion** combines early and late fusion (see Figure 1 panel 4). Initially, we use cross attention with *both*  $\mathbf{X}$  and  $\mathbf{Y}$  as the query  $Q$ : We construct a cross-shaped information flow where we embed each data source using cross-attention information from the other source. This leads to a *symmetrical* information flow and overcomes the drawback of early fusion, where one of the data sources must be chosen as the query  $Q$ . The outputs of the symmetrical cross-attention step are then each passed to an embedding network  $s_x(\cdot), s_y(\cdot)$ , and the information streams are fused just before entering the neural density estimator:

$$\begin{aligned} \tilde{\mathbf{X}} &= \text{MHA}(Q(\mathbf{X}), V(\mathbf{Y}), K(\mathbf{Y})) \\ \tilde{\mathbf{Y}} &= \text{MHA}(Q(\mathbf{Y}), V(\mathbf{X}), K(\mathbf{X})) \\ s(\mathcal{D}) &= g(s_x(\tilde{\mathbf{X}}), s_y(\tilde{\mathbf{Y}})) = [s_x(\tilde{\mathbf{X}}), s_y(\tilde{\mathbf{Y}})] \end{aligned} \quad (6)$$

We hypothesize that hybrid fusion enables more flexible resource allocation: Features of an informative source as well as interactions can be captured in the embedding network, which reduces the burden on the generative network  $q_\phi$ .

### 3.4. More than two data sources

This section will discuss the natural extension of our fusion architectures beyond two sources. In the following, let  $L \in \mathbb{N}_{\geq 2}$  be the number of data sources  $\mathcal{D} = \{\mathcal{D}_l\}_{l=1}^L$ .

Late fusion naturally translates to an arbitrary number of sources: Each source  $\mathcal{D}_l$  has a dedicated embedding network  $s_l(\mathcal{D}_l)$  to learn sufficient summary statistics for posterior inference. Finally, all embeddings are combined into a joint embedding  $s(\mathcal{D}) = g(s_1(\mathcal{D}_1), \dots, s_L(\mathcal{D}_L))$  with suitable  $g$  (e.g., concatenation as above). Thus, the number of networks in late fusion scales linearly in  $\mathcal{O}(L)$ . Early and hybrid fusion, however, involve pairwise cross-attention blocks, which do not natively generalize to  $L \geq 2$  inputs. For early fusion, there are  $L!$  options to choose the layout of pairwise cross-attention fusion blocks, but only  $1 + \dots + (L - 1)$  blocks must be realized in practice to implement a cascade of cross-attention steps for early fusion. In addition, we require one embedding network, leading to a total of  $1 + 2 + \dots + (L - 1) + 1 \in \mathcal{O}(L^2)$  networks. In hybrid fusion, however, we want a full cross-exchange of



information across all sources, which requires a total of  $L!$  networks. In addition, each source needs one embedding network. This leads to a total of  $L! + L \in \mathcal{O}(L!)$  networks, which clearly raises scaling issues for large  $L$ . Thus, a central question of this paper is to assess the extent to which the scalable late fusion approach yields similar results to the more computationally complex hybrid fusion method.

#### 4. Related work

**Multimodal fusion.** Researchers have long been integrating different types of features to improve the performance of machine learning applications (Ngiam et al., 2011). As (Guo et al., 2019) remark, using deep fusion to learn *fused representations of heterogeneous features* in multimodal settings is a natural extension of this strategy. Recently, attention-based transformer networks have been employed for multimodal problems across many applications (Xu et al., 2023), such as image and sentence matching (Wei et al., 2020), multispectral object detection (Qingyun et al., 2021), or integration of image and depth information (Gavrilyuk et al., 2020). We confirm the potential of cross-attention architectures in probabilistic machine learning with conditional neural density estimators. All of our fusion variants implement a unified embedding for heterogeneous data sources, which corresponds to *joint representation* in the taxonomy of (Guo et al., 2019).

**Multimodality and missing data.** Multimodal learning algorithms can naturally address the problem of missing data because missing information from one source may be compensated for by another source (see **Experiment 2**). In the context of multimodal time series, this has been addressed by factorized inference on state space models (Zhi-Xuan et al., 2019) and learned representations via tensor rank regularization (Liang et al., 2019). Our multimodal NPE method also learns robust representations from partially missing data, but we use fusion techniques that respect the probabilistic symmetry of the data, rather than a certain factorization of the posterior distribution. From a global angle, Bayesian meta-learning (Fei-Fei & Perona, 2005) has been used to study the efficiency of multimodal learning under missing data, both during training and inference time (Ma et al., 2021). Similarly, our approach embodies Bayesian meta-learning principles by extending the *amortization scope* of NPE to increasingly missing data, which is in turn facilitated by our fusion schemes.

**Hierarchical Bayesian models.** Hierarchical or multi-level Bayesian models (Gelman et al., 2013) are used to model the dependencies in nested data, where observations are organized into clusters or levels. While these models often feature *shared* parameters across observational units or *global* parameters describing between-cluster variations

(Wikle, 2003), they focus on analyzing the variations of a *single data modality at different levels*. In contrast, multimodal models capitalize on integrating information from different sources or modalities. That being said, a multimodal problem could also be formulated in a hierarchical way, such that the shared parameters of different modalities admit a hierarchical prior. And while the complexity of such models quickly becomes prohibitive, our MultiNPE approach could pave the way for hierarchical multimodal approaches where the latter have been foregone merely out of computational desperation.

#### 5. Empirical evaluation

**Settings.** We evaluate MultiNPE in a synthetic multimodal model with fully overlapping parameter spaces across the data modalities, a neurocognitive model with partially overlapping parameter spaces and missing data, and a cardiovascular data set with three data sources.

**Evaluation metrics.** For all experiments, we evaluate the accuracy of the posterior estimates as well as their uncertainty calibration and Bayesian information gain on  $J$  unseen test data sets  $\{\mathcal{D}_o^{(j)}\}_{j=1}^J$  with known ground-truth parameters  $\{\theta_*^{(j)}\}_{j=1}^J$ . Let  $\{\theta_s^{(j)}\}_{s=1}^S$  be the set of  $S$  posterior draws from the neural approximator  $q_\phi(\theta | \mathcal{D}_o^{(j)})$  conditioned on the data set  $\mathcal{D}_o^{(j)}$ . For accuracy, we compute the average root mean square error (RMSE) between posterior draws and ground truth parameter values over the test set:

$$\text{RMSE} = \frac{1}{J} \sum_{j=1}^J \sqrt{\frac{1}{S} \sum_{s=1}^S (\theta_s^{(j)} - \theta_*^{(j)})^2} \quad (7)$$

We quantify uncertainty calibration via simulation-based calibration (SBC; (Talts et al., 2018)): For the true posterior  $p(\theta | \mathcal{D})$ , all regions  $U_q(\theta | \mathcal{D})$  of the posterior are well calibrated for any quantile  $q \in (0, 1)$  (Bürkner et al., 2022),

$$q = \iint \mathbf{I}[\theta_* \in U_q(\theta | \mathcal{D})] p(\mathcal{D} | \theta_*) p(\theta_*) d\theta_* d\mathcal{D}, \quad (8)$$

where  $\mathbf{I}[\cdot]$  is the indicator function. Discrepancies from this equality indicate insufficient calibration of an approximate posterior. We report the median SBC error of central credible intervals computed for 20 linearly spaced quantiles  $q \in [0.5\%, 99.5\%]$ , averaged across the test set (aka. expected calibration error; ECE). Finally, we quantify the (Bayesian) information gain via posterior contraction, based on the relation between prior and posterior variance,  $1 - \text{Var}(\text{Prior}) / \text{Var}(\text{Posterior})$ , averaged across the test data. All three metrics are *global*: They estimate performance across the entire joint model  $p(\theta, \mathcal{D})$  instead of singling out particular data sets or true model parameters

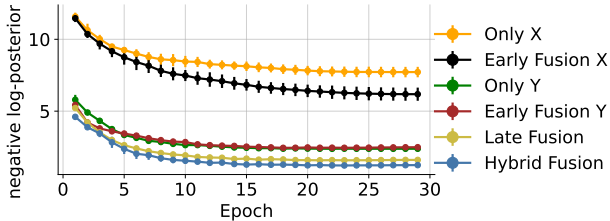


Figure 2: **Experiment 1:** Two multimodal schemes (late fusion and hybrid fusion) outperform single-source architectures (only  $\mathbf{X}/\mathbf{Y}$ ), as indexed by better (lower) negative log posterior on held-out data across ten repetitions.

(Bürkner et al., 2022). The metrics can directly be computed based on simulations from the joint model, which is essentially instantaneous due to amortized inference.

### 5.1. Exchangeable data and Brownian time series

This experiment compares MultiNPE and standard NPE on a synthetic task where a common parameter  $\theta \in \mathbb{R}^{10}$  is used as (i) the location parameter of Gaussian *i.i.d.* data  $\mathbf{X}$  and (ii) the drift rate of a stochastic trajectory  $\mathbf{Y}$ ,

$$\begin{aligned} \theta &\sim \text{Normal}(\theta \mid \mathbf{0}, \mathbf{1}), \\ \mathbf{x}_n &\sim \text{Normal}(\mathbf{x} \mid \theta, \mathbf{1}), \quad n = 1 \dots, N \\ d\mathbf{y}_m(t) &= \theta dt + \sigma d\mathbf{W}(t), \quad m = 1, \dots, M \\ &\text{with } \mathbf{W}(t) \sim \text{Normal}(\mathbf{W} \mid \mathbf{0}, \mathbf{1}), \end{aligned} \quad (9)$$

where the *i.i.d.* data consist of  $N = 5$  observations  $\mathbf{X} = \{\mathbf{x}_1, \dots, \mathbf{x}_5\}$ , the trajectory is discretized into  $M = 20$  steps  $\mathbf{Y} = (\mathbf{y}_1, \dots, \mathbf{y}_{20})$  with noise  $\sigma = 0.5$ , an interval of  $t = [0, 3]$ , and the initial condition is  $\mathbf{y}_1 = \mathbf{0}$ .

We compare the following neural approximators: NPE with input  $\mathbf{X}$ , NPE with input  $\mathbf{Y}$ , as well as MultiNPE variants with early fusion to  $\mathbf{X}$ , early fusion to  $\mathbf{Y}$ , late fusion, and hybrid fusion. Each neural approximator is trained on the same training set with a simulation budget of  $K = 5000$  for 30 epochs. All data originating from the *i.i.d.* source ( $\mathbf{X}$  or  $\tilde{\mathbf{X}}$ ) are embedded with a set transformer (Lee et al., 2019), and data on the time series stream ( $\mathbf{Y}$  or  $\tilde{\mathbf{Y}}$ ) are embedded with a temporal fusion transformer (Wen et al., 2023).

**Results.** Late fusion and hybrid fusion outperform standard NPE architectures which only have access to a single data source (see Figure 2 and Table 1). It is evident that  $\mathbf{X}$  is less informative for the posterior than  $\mathbf{Y}$  (“only  $\mathbf{X}$ ” performs much worse than “only  $\mathbf{Y}$ ”). As a consequence, early fusion to  $\mathbf{X}$  leads to worse performance than early fusion to  $\mathbf{Y}$ . We conclude that the efficacy of early fusion depends on the informativeness of the data source used as a query, which is a hyperparameter design choice that we would ideally like to circumvent. In fact, neither late nor hybrid fusion require such a design choice, and

Architecture	Time <sup>1</sup> ↓	RMSE ↓	ECE [%] ↓	Contraction ↑
Only $\mathbf{X}$	117 (110, 149)	0.81 (0.80, 0.89)	1.43 (0.98, 1.84)	0.68 (0.61, 0.68)
Only $\mathbf{Y}$	<b>100</b> (95, 141)	0.40 (0.40, 0.40)	3.44 (3.02, 3.63)	0.93 (0.93, 0.93)
Early Fusion $\mathbf{X}$	140 (131, 150)	0.88 (0.82, 0.93)	<b>1.35</b> (1.04, 1.80)	0.61 (0.57, 0.66)
Early Fusion $\mathbf{Y}$	128 (118, 152)	0.45 (0.45, 0.45)	5.45 (5.06, 5.91)	0.91 (0.91, 0.91)
Late Fusion	193 (172, 235)	0.36 (0.36, 0.36)	4.73 (4.31, 5.21)	0.94 (0.94, 0.94)
Hybrid Fusion	227 (211, 280)	<b>0.35</b> (0.35, 0.35)	4.99 (4.44, 5.18)	<b>0.95</b> (0.95, 0.95)

Table 1: **Experiment 1:** Our multimodal NPE architecture is superior to single-source NPE algorithms on 1000 unseen data sets, as indexed by improved accuracy (RMSE) and information gain (contraction). The subpar calibration under  $\mathbf{Y}$  propagates into the fused posteriors. The table shows median (min, max) across ten training runs of each architecture. <sup>1</sup> Training time [seconds]

both schemes outperform early fusion in this experiment at the cost of longer neural network training.<sup>2</sup> The most expressive neural architecture, hybrid fusion, shows the best performance by a small margin. Heuristically, it combines the best of both worlds: Hybrid fusion extracts information from the raw data by the  $\mathbf{X}$ -shaped cross-attention modules but avoids the necessity of choosing one of the domains to early-fuse into. Yet, the performance gain over late fusion is small; thus, late fusion might be employed in scenarios where practical considerations (e.g., many sources, limited time) prohibit a hybrid approach.

### 5.2. Neurocognitive model of decision making and EEG with missing data

This experiment uses a multimodal neurocognitive model that integrates both a cognitive drift-diffusion model for decision making and a representation of the neurological centroparietal positives (CPP) waveforms on an EEG (*model 7* from (Ghaderi-Kangavari et al., 2023)). A drift-diffusion model (DDM; Ratcliff & McKoon, 2008) describes a human’s decision and reaction time as a stochastic evidence accumulation process with explainable parameters (for a detailed description, see Voss et al., 2004). In contrast to the behavioral reaction time data of the DDM, the CPP waveform is a neural marker that is associated with human decision making (Ghaderi-Kangavari et al., 2023). In this setting, we study the potential of MultiNPE to tackle (i) partially overlapping parameter spaces; and (ii) missing

<sup>2</sup>While the training time scales linearly with the number of multi-head attention modules, the summary networks are also based on self-attention. Thus, *runtime complexity* is unaffected by our additional fusion scheme.

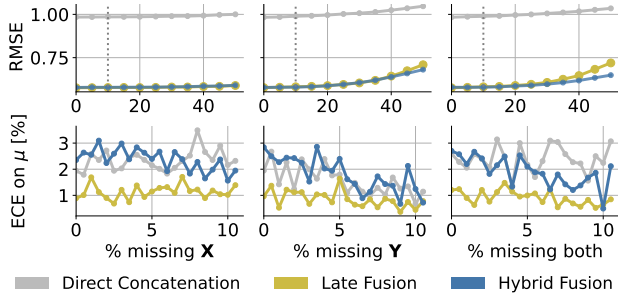


Figure 3: **Experiment 2:** Hybrid fusion and late fusion consistently show better accuracy (RMSE averaged over all parameters) than the default (direct concatenation). Recall that the training uses 10% missing data (top row, dotted line) and missingness beyond 10% is a substantial extrapolation. Calibration (ECE) of the shared parameter  $\mu$  does not clearly differ between the methods.

data. The forward model is parameterized by six parameters (defined below) that govern two partially entangled data generating processes on a trial-by-trial level,

$$\begin{aligned}
 \mu, \sigma, \alpha, \tau, \beta, \eta &\sim p(\mu, \sigma, \alpha, \tau, \beta, \eta) && \text{(prior)} \\
 v_n &\sim \text{Normal}(v \mid \mu, \sigma) && \text{(per-trial entanglement)} \\
 \mathbf{x}_n &\sim \text{DDM}(\mathbf{x} \mid \alpha, \tau, v_n, \beta) && \text{(reaction time)} \\
 \mathbf{y}_n &\sim \text{Normal}(\mathbf{y} \mid v_n, \eta) && \text{(CPP waveform)}
 \end{aligned} \tag{10}$$

with shared *global* information uptake rate  $\mu$  and associated error  $\sigma$ . In this model,  $\text{DDM}(\mathbf{x} \mid \cdot)$  is a drift-diffusion model (Voss et al., 2004). Further,  $\text{Normal}(\mathbf{y} \mid \cdot)$  represents the neurocognitive CPP model from Ghaderi-Kangavari et al. (2023). Crucially, the data sources are entangled on the trial level since the shared information uptake rate  $v_n$  is sampled for each experimental trial  $n$ . This implies an equal number of observations for both sources, corresponding to the number of trials,  $N=M=200$ , per data set  $\mathcal{D}^{(k)} = \{\mathbf{X}^{(k)}, \mathbf{Y}^{(k)}\}$ . To synthetically induce missing data, we uniformly sample missing rates between 1% and 10% for each training batch and encode missingness as in (Wang et al., 2023). With a simulation budget of  $K=4096$ , we compare direct concatenation<sup>3</sup> (default), late fusion, and hybrid fusion.

**Results.** As displayed in Figure 3, both late fusion and hybrid fusion outperform direct concatenation via increased accuracy (RMSE) across all missing data rates. The calibration (ECE) on the shared information uptake parameter  $\mu$  does not differ between the methods. This underscores the potential of deep fusion in SBI even in situations

<sup>3</sup>Direct concatenation on the data level is possible because  $\mathbf{X}$  and  $\mathbf{Y}$  have identical structure. Thus, there is no necessity for early fusion. We directly concatenate  $\mathbf{X}$  and  $\mathbf{Y}$  and use a single embedding network.

Architecture	Time <sup>1</sup> ↓	RMSE ↓	ECE [%] ↓	Contraction ↑	
Affine Flow	Only $\mathbf{X}$	1296	0.94	1.90	0.53
	Only $\mathbf{Y}$	1307	1.05	1.38	0.39
	Only $\mathbf{Z}$	1202	0.90	3.47	0.55
	Late Fusion	2010	<b>0.45</b>	5.25	<b>0.90</b>
	Hybrid Fusion	2761	0.75	1.33	0.68
Spline Flow	Only $\mathbf{X}$	1991	1.08	1.27	0.37
	Only $\mathbf{Y}$	2028	1.05	0.82	0.39
	Only $\mathbf{Z}$	1993	1.18	0.97	0.24
	Late Fusion	1880	0.87	<b>0.67</b>	0.56
	Hybrid Fusion	3612	0.64	1.62	0.75
Flow Matching	Only $\mathbf{X}$	1040	0.55	6.93	0.85
	Only $\mathbf{Y}$	1155	0.67	6.29	0.78
	Only $\mathbf{Z}$	<b>993</b>	0.83	8.30	0.72
	Late Fusion	2668	0.50	8.24	0.87
	Hybrid Fusion	4208	0.62	5.98	0.81

Table 2: **Experiment 3:** Test set performance of different generative models (affine flow, spline flow, flow matching) and fusion strategies (single sources, late fusion, hybrid fusion). Taking all three metrics into account, affine flows with late fusion or hybrid fusion yield the best results. <sup>1</sup> Training time [seconds].

where the fusion architectures do not have access to more raw data because the naïve approach (i.e., direct concatenation) is possible due to compatible input shapes of the data sources. We hypothesize that our fusion scheme embodies a favorable inductive bias by separating the data sources.

### 5.3. Cardiovascular in-silico model with 3 sources

Preventing cardiovascular diseases is a fundamental challenge of precision medicine, and scientific hemodynamics simulators are a key to understanding the cardiovascular system (Ashley, 2016). The *pulse wave database* (Charlton et al., 2019) contains data from 4374 in-silico subjects, validated with in-vivo data. A whole-body simulator models the hemodynamics of the 116 largest human arteries via differential equations and contains measurements of a single heart beat at different locations in the human body, including both photoplethysmograms (PPG) and arterial pressure waveform (APW). Data from the pulse wave database has been previously analyzed with unimodal SBI methods (Wehenkel et al., 2023), and our experiment is closely inspired by this work. We consider the following measurements as individual data sources  $\mathcal{D} = \{\mathbf{X}, \mathbf{Y}, \mathbf{Z}\}$ : PPG at the digital artery ( $\mathbf{X}$ ), PPG at the radial artery ( $\mathbf{Y}$ ), and APW at the radial artery ( $\mathbf{Z}$ ). The shared parameters  $\theta$  in this experiment consist of the left ventricular ejection time (LVET), the systemic vascular resistance (SVR), the average diameter of arteries, and the pulse wave velocity.

As an extension to (Wehenkel et al., 2023), we employ the challenging and realistic setting where measurements

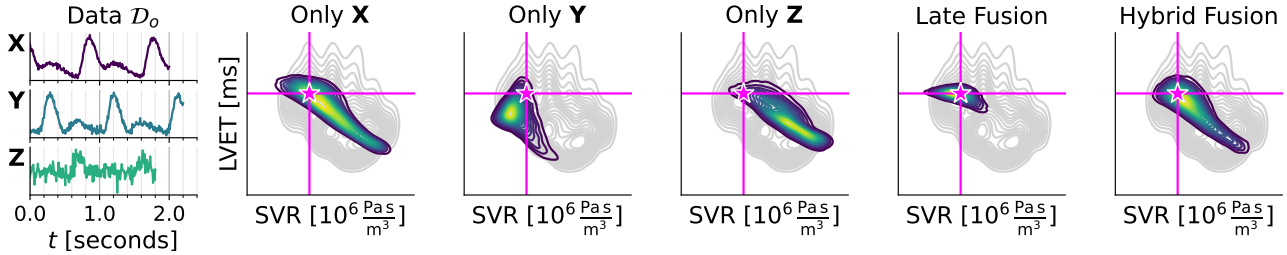


Figure 4: **Experiment 3:** Bivariate posterior plots of SVR and LVET for one unseen data set  $\mathcal{D}_o$  (left), as obtained by NPE with affine flows. We show the implicit prior density (gray), the ground-truth  $\theta_*$  (magenta), and a KDE over 10 000 approximate posterior samples (viridis). Posteriors from late fusion and hybrid fusion are more concentrated at the ground-truth compared to the single-source methods.

from different devices ( $\mathbf{X}$ ,  $\mathbf{Y}$ ,  $\mathbf{Z}$ ) are not synchronized in time (see Figure 4, left, for an example). Concretely, we achieve this with a two-step process: First, we loop the single-beat signals to a longer sequence and crop the sequence into a fixed-length measurement interval for each subject. The length of the cropped signal differs between the sources ( $\mathbf{X}$ : 2.0 seconds,  $\mathbf{Y}$ : 2.2 seconds,  $\mathbf{Z}$ : 1.8 seconds). The sequence onset times are randomly sampled for each subject and source, which means that the cropped signals are not synchronized anymore within each subject. Second, we add Gaussian white noise to the signals, and the signal-to-noise (SNR) ratio is specific for each data source ( $\mathbf{X}$ : 25dB,  $\mathbf{Y}$ : 20dB,  $\mathbf{Z}$ : 30dB). This emulates different measurement devices in a hospital, where each device has a specific measurement error. In this realistic setting, we cannot simply concatenate the inputs, but instead require fusion schemes to integrate the heterogeneous cardiovascular measurements  $\mathbf{X}$ ,  $\mathbf{Y}$ ,  $\mathbf{Z}$ .

Since the data are only available as an offline data set and not as a simulation program, we face a scenario with both an implicit likelihood and an implicit prior. Further, a subject’s age is a key factor for cardiovascular health in the pulse wave database (Charlton et al., 2019). Thus, we follow Wehenkel et al. (2023) and use age as an additional direct condition (i.e., without embedding) for the neural density estimator. We compare the performance of single-source models (i.e., only access to  $\mathbf{X}$ ,  $\mathbf{Y}$ , or  $\mathbf{Z}$ ) to our multimodal variants late fusion and hybrid fusion. Since simulation-based posterior estimation for this data set is a challenging problem by itself, we further employ each strategy with three different generative models: (i) affine flows (Dinh et al., 2016); (ii) neural spline flows (Durkan et al., 2019); and (iii) flow matching (Liu et al., 2022).

**Results.** Overall, affine flows emerge as the best generative model in this experiment, closely followed by flow matching (see Table 2). The subpar performance of spline flows may be related to the relatively large data dimension in conjunction with the probabilistic geometry of the noisy

time series data. Within both affine flows and flow matching, late fusion shows the best combination of high accuracy and information gain, but suffers from poor calibration. As opposed to Experiment 1, late fusion and hybrid fusion differ with respect to their performance profile: While late fusion yields superior accuracy and contraction, it does not reach the calibration quality of hybrid fusion. Thus, we conclude that affine flows with either late fusion or hybrid fusion are desirable in this application from precision medicine, and both fusion schemes have a *raison d’être* in challenging real-life scenarios. Finally, we illustrate the *bivariate* posterior of a parameter subspace of practical interest, namely that of SVR and LVET (Wehenkel et al., 2023), under different fusion schemes in Figure 4. Given one unseen data set  $\mathcal{D}_o$  and an affine flow backbone, the approximate posteriors of our deep fusion schemes concentrate around the true parameter value  $\theta_*$  more strongly than single-source NPE. The Appendix contains bivariate posteriors for all generative architectures and further test data sets.

## 6. Conclusion

We presented MultiNPE, a new multimodal approach to perform simulation-based Bayesian inference for models with heterogeneous data generating processes. MultiNPE seamlessly integrates information from heterogeneous sources, which is unattainable with conventional neural posterior estimators. We applied MultiNPE to a 10-dimensional benchmark task, an integrative model from cognitive neuroscience with missing data, and a cardiovascular model with different emulated measurement devices in a hospital. Overall, our results underscore the potential of MultiNPE as a novel simulation-based inference tool for real-world problems with multiple data sources. It pushes the boundaries of modern simulation-based inference with neural networks and further paves the way for its widespread application in science and engineering. The FAQ section in the Appendix answers some questions we encountered prior to submission.



## Impact statement

This paper presents work whose goal is to advance the field of machine learning. There are many potential societal consequences of our work, none of which we feel must be specifically highlighted here.

## Acknowledgments

We thank Lasse Elsemüller for insightful feedback and input on the manuscript. MS thanks the Cyber Valley Research Fund (grant number: CyVy-RF-2021-16), the Deutsche Forschungsgemeinschaft (DFG, German Research Foundation) under Germany’s Excellence Strategy EXC-2075 - 390740016 (the Stuttgart Cluster of Excellence SimTech), the Google Cloud Research Credits program, and the European Laboratory for Learning and Intelligent Systems (ELLIS) PhD program for support.

## References

- Ashley, E. A. Towards precision medicine. *Nature Reviews Genetics*, 17(9):507–522, 2016. doi: 10.1038/nrg.2016.86. URL <https://doi.org/10.1038/nrg.2016.86>.
- Atrey, P. K., Hossain, M. A., Saddik, A. E., and Kankanhalli, M. S. Multimodal fusion for multimedia analysis: a survey. *Multimedia Systems*, 16(6):345–379, April 2010. doi: 10.1007/s00530-010-0182-0. URL <https://doi.org/10.1007/s00530-010-0182-0>.
- Blei, D. M., Kucukelbir, A., and McAuliffe, J. D. Variational inference: A review for statisticians. *Journal of the American statistical Association*, 112(518):859–877, 2017.
- Bürkner, P.-C., Scholz, M., and Radev, S. T. Some models are useful, but how do we know which ones? towards a unified bayesian model taxonomy, 2022.
- Chan, J., Perrone, V., Spence, J., Jenkins, P., Mathieson, S., and Song, Y. A likelihood-free inference framework for population genetic data using exchangeable neural networks. *Advances in neural information processing systems*, 31, 2018.
- Charlton, P. H., Harana, J. M., Vennin, S., Li, Y., Chowienczyk, P., and Alastruey, J. Modeling arterial pulse waves in healthy aging: a database for in silico evaluation of hemodynamics and pulse wave indexes. *American Journal of Physiology-Heart and Circulatory Physiology*, 317(5):H1062–H1085, 2019. doi: 10.1152/ajpheart.00218.2019. URL <https://doi.org/10.1152/ajpheart.00218.2019>.
- Chen, Y., Zhang, D., Gutmann, M. U., Courville, A., and Zhu, Z. Neural approximate sufficient statistics for implicit models. In *International Conference on Learning Representations*, 2021. URL <https://openreview.net/forum?id=SRDuJssQud>.
- Cranmer, K., Brehmer, J., and Louppe, G. The frontier of simulation-based inference. *Proceedings of the National Academy of Sciences*, 2020.
- Dax, M., Wildberger, J., Buchholz, S., Green, S. R., Macke, J. H., and Schölkopf, B. Flow matching for scalable simulation-based inference, 2023.
- Dinh, L., Sohl-Dickstein, J., and Bengio, S. Density estimation using real NVP. *arXiv preprint arXiv:1605.08803*, 2016.
- Dosovitskiy, A., Beyer, L., Kolesnikov, A., Weissenborn, D., Zhai, X., Unterthiner, T., Dehghani, M., Minderer, M., Heigold, G., Gelly, S., Uszkoreit, J., and Houlsby, N. An image is worth 16x16 words: Transformers for image recognition at scale. In *International Conference on Learning Representations*, 2021. URL <https://openreview.net/forum?id=YicbFdNTTy>.
- Durkan, C., Bekasov, A., Murray, I., and Papamakarios, G. Neural spline flows. *Advances in neural information processing systems*, 32, 2019.
- Fei-Fei, L. and Perona, P. A bayesian hierarchical model for learning natural scene categories. In *2005 IEEE Computer Society Conference on Computer Vision and Pattern Recognition (CVPR’05)*, volume 2, pp. 524–531 vol. 2, 2005. doi: 10.1109/CVPR.2005.16.
- Gavrilyuk, K., Sanford, R., Javan, M., and Snoek, C. G. M. Actor-transformers for group activity recognition. In *2020 IEEE/CVF Conference on Computer Vision and Pattern Recognition (CVPR)*, pp. 836–845, 2020. doi: 10.1109/CVPR42600.2020.00092.
- Geffner, T., Papamakarios, G., and Mnih, A. Compositional score modeling for simulation-based inference, 2022.
- Gelman, A., Carlin, J. B., Stern, H. S., Dunson, D. B., Vehtari, A., and Rubin, D. B. *Bayesian Data Analysis (3rd Edition)*. Chapman and Hall/CRC, 2013.
- Ghaderi-Kangavari, A., Rad, J. A., and Nunez, M. D. A general integrative neurocognitive modeling framework to jointly describe EEG and decision-making on single trials. *Computational Brain and Behavior*, 2023. doi: 10.1007/s42113-023-00167-4.
- Gunes, H. and Piccardi, M. Affect recognition from face and body: Early fusion vs. late fusion. In *2005*

- IEEE International Conference on Systems, Man and Cybernetics*. IEEE, 2005. doi: 10.1109/icsmc.2005.1571679. URL <https://doi.org/10.1109/icsmc.2005.1571679>.
- Guo, W., Wang, J., and Wang, S. Deep multimodal representation learning: A survey. *IEEE Access*, 7:63373–63394, 2019. doi: 10.1109/access.2019.2916887. URL <https://doi.org/10.1109/access.2019.2916887>.
- Hochreiter, S. and Schmidhuber, J. Long short-term memory. *Neural computation*, 9(8):1735–1780, 1997.
- Huang, D., Bharti, A., Souza, A., Acerbi, L., and Kaski, S. Learning robust statistics for simulation-based inference under model misspecification, 2023.
- Lavin, A., Zenil, H., Paige, B., et al. Simulation intelligence: Towards a new generation of scientific methods. *arXiv preprint*, 2021.
- Lee, J., Lee, Y., Kim, J., Kosiorek, A., Choi, S., and Teh, Y. W. Set transformer: A framework for attention-based permutation-invariant neural networks. In Chaudhuri, K. and Salakhutdinov, R. (eds.), *Proceedings of the 36th International Conference on Machine Learning*, volume 97 of *Proceedings of Machine Learning Research*, pp. 3744–3753. PMLR, 09–15 Jun 2019. URL <https://proceedings.mlr.press/v97/lee19d.html>.
- Liang, P. P., Liu, Z., Tsai, Y.-H. H., Zhao, Q., Salakhutdinov, R., and Morency, L.-P. Learning representations from imperfect time series data via tensor rank regularization, 2019.
- Liu, X., Gong, C., and Liu, Q. Flow straight and fast: Learning to generate and transfer data with rectified flow, 2022.
- Lu, J., Batra, D., Parikh, D., and Lee, S. *ViLBERT: Pre-training Task-Agnostic Visiolinguistic Representations for Vision-and-Language Tasks*. Curran Associates Inc., Red Hook, NY, USA, 2019.
- Ma, M., Ren, J., Zhao, L., Tulyakov, S., Wu, C., and Peng, X. Smil: Multimodal learning with severely missing modality, 2021.
- Murahari, V., Batra, D., Parikh, D., and Das, A. Large-scale pretraining for visual dialog: A simple state-of-the-art baseline. In Vedaldi, A., Bischof, H., Brox, T., and Frahm, J.-M. (eds.), *Computer Vision – ECCV 2020*, pp. 336–352, Cham, 2020. Springer International Publishing. ISBN 978-3-030-58523-5.
- Neal, R. M. *MCMC using Hamiltonian dynamics*. May 2011. doi: 10.1201/b10905.
- Ngiam, J., Khosla, A., Kim, M., Nam, J., Lee, H., and Ng, A. Y. Multimodal deep learning. In *Proceedings of the 28th International Conference on International Conference on Machine Learning, ICML’11*, pp. 689–696, Madison, WI, USA, 2011. Omnipress. ISBN 9781450306195.
- Papamakarios, G., Nalisnick, E., Rezende, D. J., Mohamed, S., and Lakshminarayanan, B. Normalizing flows for probabilistic modeling and inference. *J. Mach. Learn. Res.*, 22(1), jan 2021. ISSN 1532-4435.
- Qingyun, F., Dapeng, H., and Zhaokui, W. Cross-modality fusion transformer for multispectral object detection, 2021.
- Radev, S. T., Mertens, U. K., Voss, A., Ardizzone, L., and Köthe, U. BayesFlow: Learning complex stochastic models with invertible neural networks. *IEEE transactions on neural networks and learning systems*, 2020a.
- Radev, S. T., Mertens, U. K., Voss, A., and Köthe, U. Towards end-to-end likelihood-free inference with convolutional neural networks. *British Journal of Mathematical and Statistical Psychology*, 73(1):23–43, 2020b.
- Ratcliff, R. and McKoon, G. The diffusion decision model: Theory and data for two-choice decision tasks. *Neural Computation*, 20(4):873–922, 2008.
- Schmitt, M., Bürkner, P.-C., Köthe, U., and Radev, S. T. Detecting model misspecification in amortized Bayesian inference with neural networks. *arXiv preprint*, 2021.
- Schmitt, M., Pratz, V., Köthe, U., Bürkner, P.-C., and Radev, S. T. Consistency models for scalable and fast simulation-based inference, 2023. arXiv:2312.05440.
- Sharrock, L., Simons, J., Liu, S., and Beaumont, M. Sequential neural score estimation: Likelihood-free inference with conditional score based diffusion models, 2022.
- Sisson, S. A., Fan, Y., and Beaumont, M. *Handbook of approximate Bayesian computation*. CRC Press, 2018.
- Talts, S., Betancourt, M., Simpson, D., Vehtari, A., and Gelman, A. Validating Bayesian inference algorithms with simulation-based calibration. *arXiv preprint*, 2018.
- Vaswani, A., Shazeer, N., Parmar, N., Uszkoreit, J., Jones, L., Gomez, A. N., Kaiser, L. u., and Polosukhin, I. Attention is all you need. In Guyon, I., Luxburg, U. V., Bengio, S., Wallach, H., Fergus, R., Vishwanathan, S., and Garnett, R. (eds.), *Advances in Neural Information*

*Processing Systems*, volume 30. Curran Associates, Inc., 2017.

Voss, A., Rothermund, K., and Voss, J. Interpreting the parameters of the diffusion model: An empirical validation. *Memory & Cognition*, 32(7):1206–1220, 2004.

Wang, Z., Hasenauer, J., and Schälte, Y. Missing data in amortized simulation-based neural posterior estimation. 2023. doi: 10.1101/2023.01.09.523219. URL <https://doi.org/10.1101/2023.01.09.523219>.

Wehenkel, A., Behrmann, J., Miller, A. C., Sapiro, G., Sener, O., Cuturi, M., and Jacobsen, J.-H. Simulation-based inference for cardiovascular models, 2023.

Wei, X., Zhang, T., Li, Y., Zhang, Y., and Wu, F. Multi-modality cross attention network for image and sentence matching. In *2020 IEEE/CVF Conference on Computer Vision and Pattern Recognition (CVPR)*. IEEE, June 2020. doi: 10.1109/cvpr42600.2020.01095. URL <https://doi.org/10.1109/cvpr42600.2020.01095>.

Wen, Q., Zhou, T., Zhang, C., Chen, W., Ma, Z., Yan, J., and Sun, L. Transformers in time series: A survey. In *International Joint Conference on Artificial Intelligence (IJCAI)*, 2023.

Wikle, C. K. Hierarchical bayesian models for predicting the spread of ecological processes. *Ecology*, 84(6): 1382–1394, 2003.

Xu, P., Zhu, X., and Clifton, D. A. Multimodal learning with transformers: A survey. *IEEE Transactions on Pattern Analysis and Machine Intelligence*, 45(10): 12113–12132, oct 2023. ISSN 1939-3539. doi: 10.1109/TPAMI.2023.3275156.

Zaheer, M., Kottur, S., Ravanbakhsh, S., Poczos, B., Salakhutdinov, R., and Smola, A. Deep sets, 2017.

Zhang, C., Yang, Z., He, X., and Deng, L. Multimodal intelligence: Representation learning, information fusion, and applications. 2019. doi: 10.1109/JSTSP.2020.2987728.

Zhi-Xuan, T., Soh, H., and Ong, D. C. Factorized inference in deep markov models for incomplete multimodal time series, 2019.

## A. Frequently Asked Questions (FAQ)

**Q:** Can't you just train the summary networks in isolation? Why would you train them jointly with the normalizing flow?

**A:** This is not generally possible because we are interested in (learned) summary statistics that are optimal for *posterior inference*. The summaries are not meant to reconstruct the data. Thus, it is paramount that the summary network(s) and the neural density estimator are trained end-to-end.

**Q:** Why did you choose these tasks? Isn't there a benchmark suite for multimodal simulation-based inference?

**A:** Since this paper is pioneering the joint analysis of heterogeneous data sources in simulation-based inference, there is no established benchmark suite to use. We aimed to cover a wide range of practically relevant cases with our selected experiments, ranging from a toy example (**Experiment 1**), to a practically important missing data setting on a recent cognitive model (**Experiment 2**), to in-silico cardiovascular data with realistic challenged (**Experiment 3**).

**Q:** Why aren't you benchmarking against a set of other multimodal SBI methods?

**A:** See above, our work is the first SBI method for fusing heterogeneous data. We compare our approach with single-source methods in **Experiments 1 and 3**, and we specifically designed **Experiment 2** such that the naïve SBI approach can handle the two-source input if the data are concatenated.

**Q:** Can the method be applied to other multimodal data sets like text and images?

**A:** While that's theoretically possible for our deep fusion schemes, the simulation-based inference approach with full uncertainty quantification will likely not scale to such data at the frontier of generative AI research.

## B. Implementation details

All experiments are performed on a machine with 4 vCPUs, an NVIDIA T4 GPU, and 15GB RAM.

### B.1. Experiment 1

**Neural network details** All transformer embedding networks use 4 attention heads, 32-dimensional keys, 10% dropout, layer normalization, 2 fully-connected layers of 64 units each within the attention heads, and learn 10-dimensional embeddings. The multihead-attention blocks for early fusion and the early stage of hybrid fusion use 4 attention heads, 32-dimensional keys, 10% dropout, layer normalization, and 3 fully-connected layers of 64 units each within the attention heads. The conditional normalizing flow consists of 8 affine coupling layers, each with one fully-connected layer of 32 units and an L2 kernel regularizer with weight  $\gamma = 10^{-4}$ . Across all architectures, we use an initial learning rate of  $10^{-4}$  with cosine decay, a batch size of 32, and train for 30 epochs without early stopping.

### B.2. Experiment 2

The prior distributions for the parameters are defined as

$$\begin{aligned}
 \mu &\sim \mathcal{U}(0.1, 3), \\
 \alpha &\sim \mathcal{U}(0.5, 2), \\
 \beta &\sim \mathcal{U}(0.1, 0.9), \\
 \tau &\sim \mathcal{U}(0.1, 1), \\
 \sigma &\sim \mathcal{U}(0, 2), \\
 \eta &\sim \mathcal{U}(0, 2),
 \end{aligned} \tag{11}$$

where  $\mathcal{U}(a, b)$  denotes the uniform distribution with lower bound  $a$  and upper bound  $b$ .

**Missing data** We synthetically induce missing data in the data generating process by uniformly sampling individual missing rates  $\rho_x, \rho_y \in [0.01, 0.10]^2$  for each batch during training. Subsequently, we create two independent masks  $m_x \sim \text{Bernoulli}(1 - \rho_x)$  and  $m_y \sim \text{Bernoulli}(1 - \rho_y)$  which determine whether each data set is missing or not. As proposed by (Wang et al., 2023) for simulation-based inference, we encode missing data as a constant  $\mathbf{c}$  with measure zero under the data generating process,  $\mathbf{c} = -1.0, p(\mathbf{c}) = 0$ . Additionally, we append the masks  $m_x, m_y$  to the data  $\mathbf{X}, \mathbf{Y}$ , which has been shown to facilitate discrimination between available and missing data for the neural density estimator



(Wang et al., 2023).

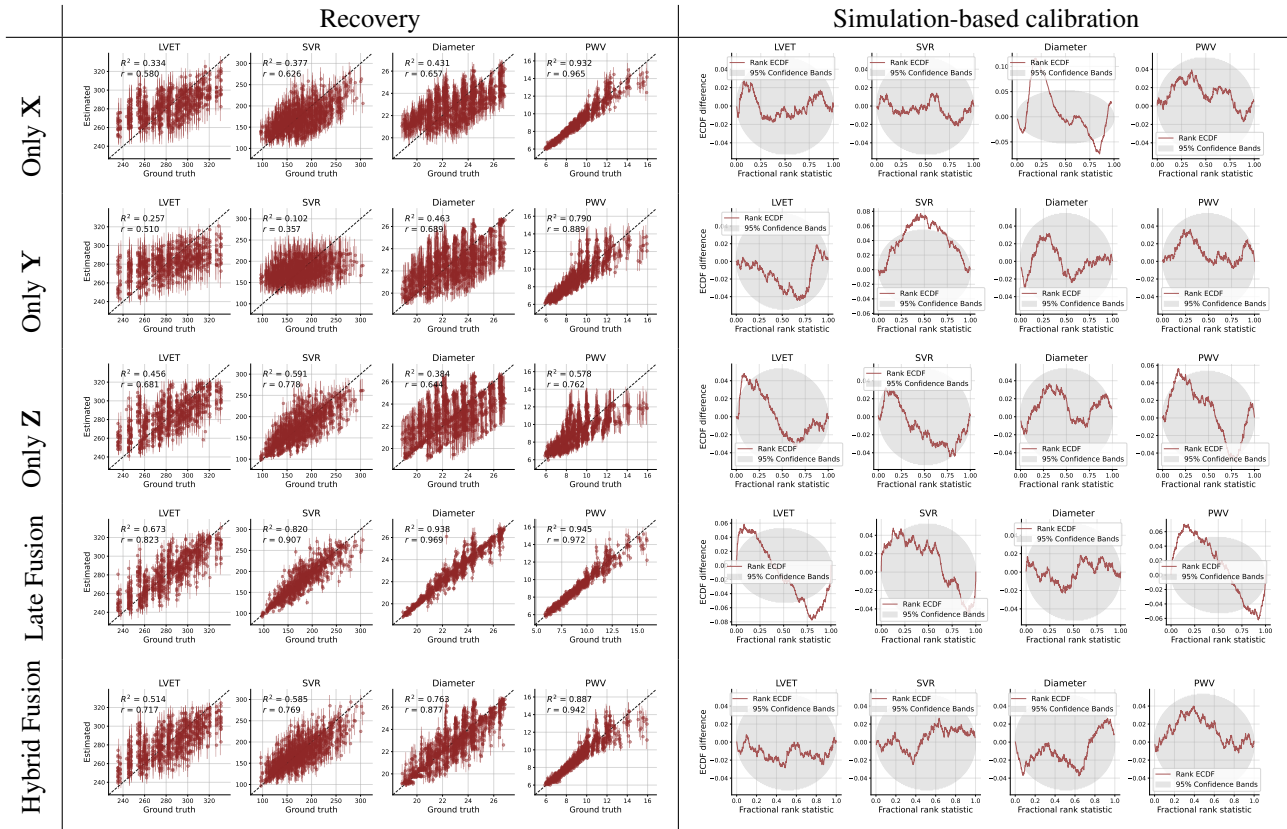
**Neural network details** The multi-head attention blocks for early fusion and hybrid fusion use no layer normalization. The embedding networks are equivariant set transformers with 2 self-attention blocks of 4 attention heads, 64-dimensional keys and 10% dropout. The number of learned embeddings equals 12, which implements the heuristic from (Schmitt et al., 2021) to use twice the number of inference target parameters. The neural density estimator is a neural spline flow with 4 coupling blocks, each consisting of 3 dense blocks with 128 units, L2 kernel regularization with weight  $\gamma = 10^{-4}$ , 10% dropout, and spectral normalization to further support learning in low data regimes with missing data. All networks train for 100 epochs with a batch size of 32.

### B.3. Experiment 3

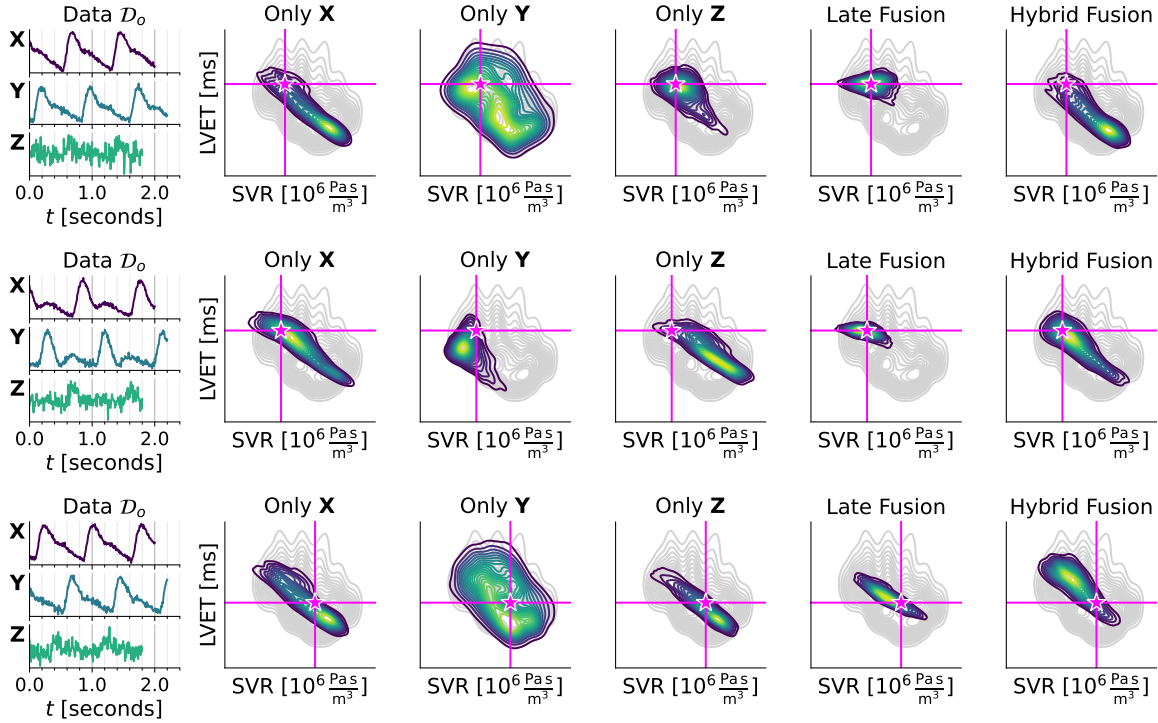
In addition to the preprocessing steps outlined in the main text, we downsample the original 500Hz signal from the pulse-wave database to 125Hz with the naïve method of using only every 4<sup>th</sup> measurement. Further, we normalize data and parameters with respect to the empirical mean and standard deviation of the training set. In order to employ temporal fusion transformers as summary networks, we add a linear time encoding to the data, which is not synchronized between sources.

**Neural network details** The multi-head attention blocks in early fusion and hybrid fusion use 4 attention heads, 32-dimensional keys, 1% dropout, and layer normalization. The temporal fusion transformers that we employ as summary networks for time series data use 2 multi-head self-attention blocks with 4 attention heads each, 32-dimensional keys, 10% dropout, and layer normalization. The embedding networks learn 30-dimensional representations (aka. summary statistics or features). Both the affine coupling flow and the neural spline flow use 8 coupling blocks, each featuring 2 dense layers of 64 units, 10% dropout, and an L2 kernel regularizer with weight  $\gamma = 10^{-4}$ . Flow matching uses a drift network with two dense layers of 64 units, 10% dropout and an L2 kernel regularizer with weight  $\gamma = 10^{-4}$ . All architectures use a batch size of 16 and an initial learning rate of  $5 \cdot 10^{-4}$  with subsequent cosine decay. We train the affine coupling flow and neural spline flow for 100 epochs, while flow matching trains for 200 epochs.

**Additional detailed results** In addition to the bivariate posterior plots in the main text, we show results for further test instances and all three neural density estimators. Additionally, we report additional results on the closed-world performance over the entire test set, namely the (i) parameter recovery (ground-truth vs. estimated); and (ii) detailed simulation-based calibration (SBC) analyses (see Figure 5, 6, 7).

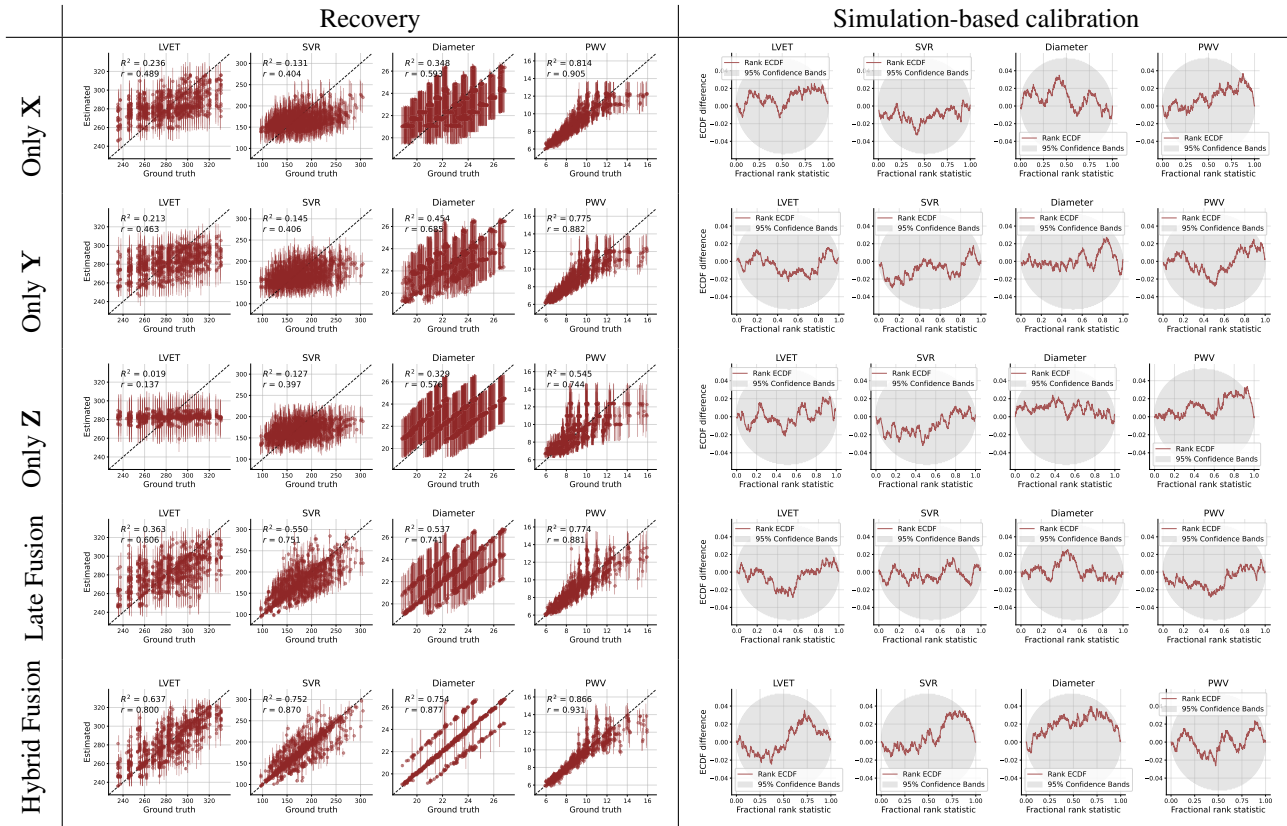


(a) Recovery and simulation-based calibration across the test set

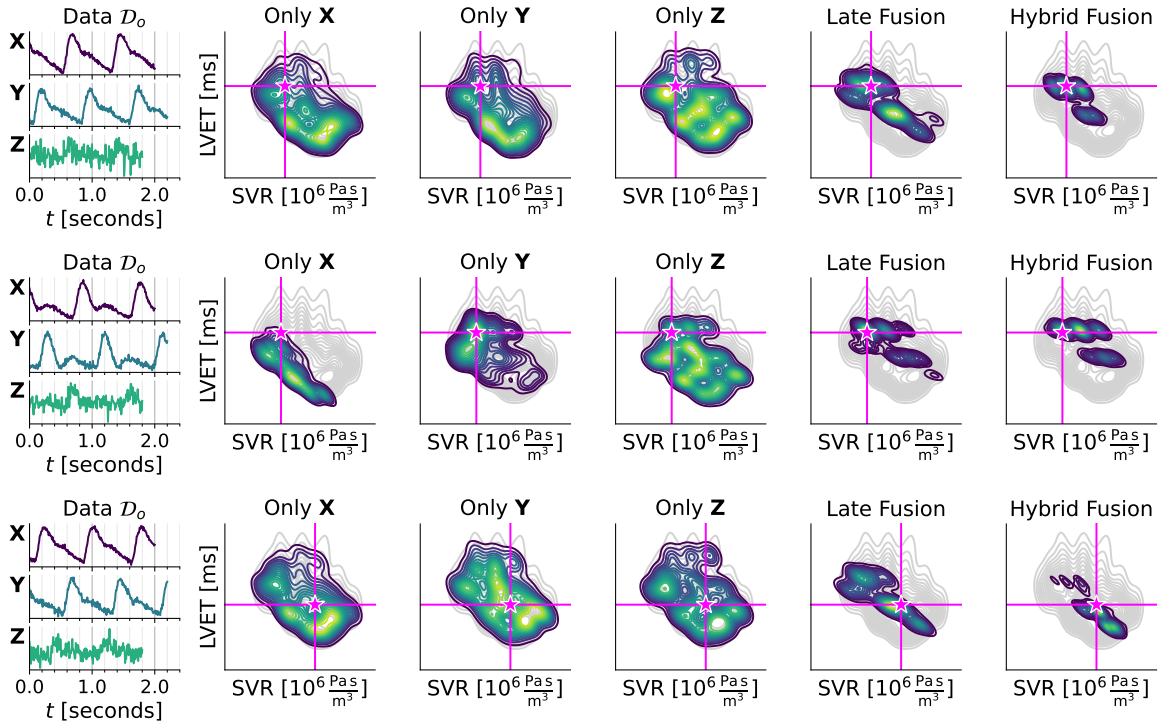


(b) Bivariate posterior plots on further test instances

Figure 5: Experiment 3, affine coupling flow.

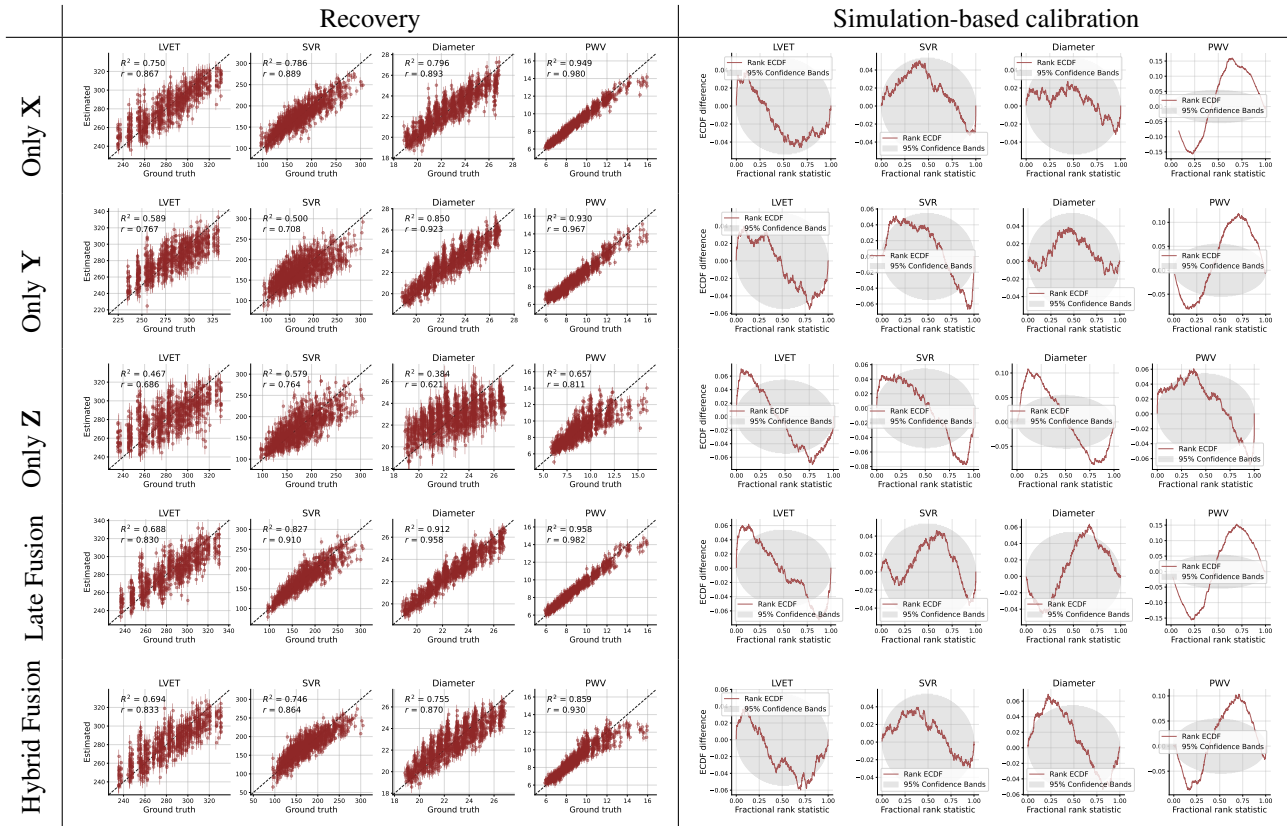


(a) Recovery and simulation-based calibration across the test set

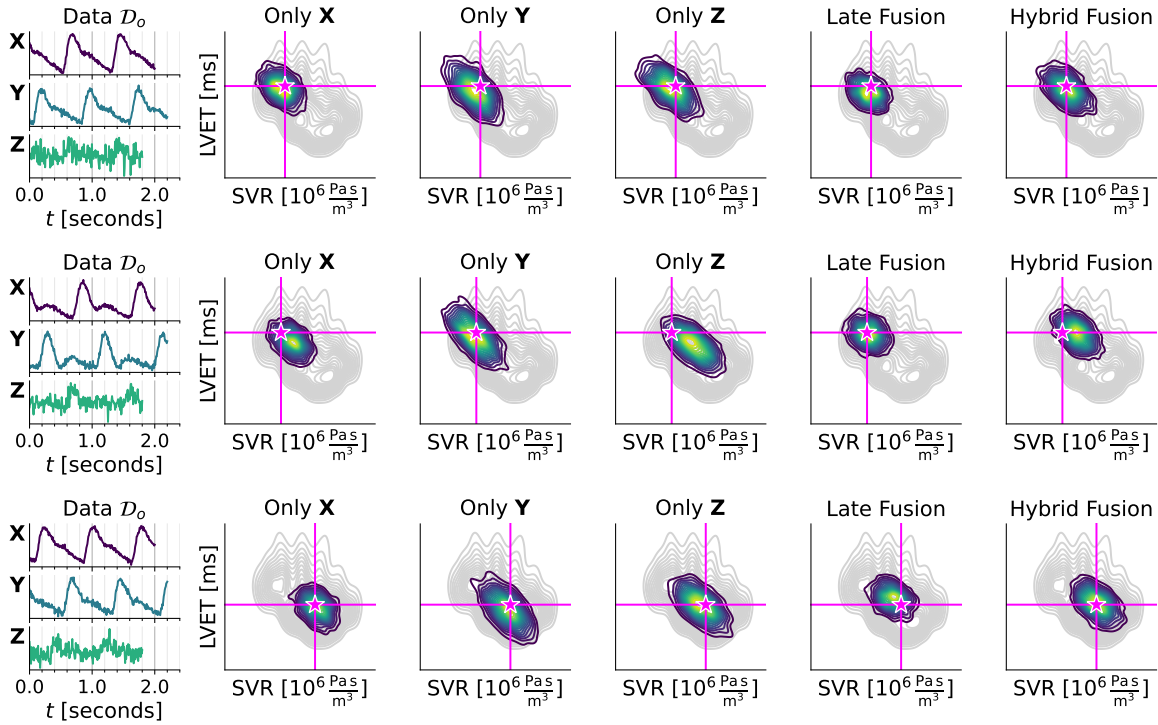


(b) Bivariate posterior plots on further test instances

Figure 6: Experiment 3, neural spline flow.



(a) Recovery and simulation-based calibration across the test set



(b) Bivariate posterior plots on further test instances

Figure 7: Experiment 3, flow matching.